Sensors and Actuators B 208 (2015) 112–121

Contents lists available at ScienceDirect

Sensors and Actuators B: Chemical

journal homepage: www.elsevier.com/locate/snb

Fabrication of gas sensor based on mesoporous rhombus-shaped ZnO rod arrays

Zhen Wen, Liping Zhu*, Ziyue Zhang, Zhizhen Ye

State Key Laboratory of Silicon Materials, Department of Materials Science and Engineering, Cyrus Tang Center for Sensor Materials and Applications, Zhejiang University, Hangzhou 310027, PR China

ARTICLE INFO

Article history:
Received 2 September 2014
Received in revised form 3 November 2014
Accepted 5 November 2014
Available online 13 November 2014

Keywords:
Gas sensor
Mesoporous
Zinc oxide
Rod arrays
Annealing temperature
High performance

ABSTRACT

Mesoporous rhombus-shaped ZnO rod arrays based gas sensors were successfully fabricated by a post-thermal conversion of rhombic Zn(OH)F precursors after a low temperature fluorine-mediated hydrothermal method. The gas sensors annealed at 350, 450, 550 and 650 °C showed different responses for ethanol detection. Increasing of the annealing temperatures resulted in the decline of gas response, which is due to the effect of grain size distributions, specific surface area and defect concentration. At low temperature (less than 350 °C), the incomplete decomposition of Zn(OH)F led to the instability of the sensors. The sensor annealed at 450 °C showed the best performance, and the response to 100 ppm ethanol reached ~11.8 at 300 °C. The sensor also exhibited good response/recovery speed (4 s and 7 s), excellent gas response and good stability. The fabrication of the high-performance gas sensors possesses the capability of constructing complex architectures with mesoporous rhombus-shaped ZnO rod arrays as the building block.

© 2014 Elsevier B.V. All rights reserved.

1. Introduction

Metal oxide semiconductor gas sensors have gained special focus due to their unique properties and application [1–3]. With the development of nano-science and technology, a large number of one-dimensional (1D) semiconductor nanostructured materials for fabricating various gas sensors (nanorods, nanowires, nanoneedles and nanotubes) have attracted considerable attention due to their large surface area, morphological control and superior charge transport [4–7]. From the viewpoint of device structure, metal oxide semiconductor-based gas sensors have been usually synthesized in the form of thin films, in which the powders are screen printed on prefabricated electrodes ceramics tubes or insulative plates followed by annealing at appropriate temperature. Nevertheless, only a small fraction of the species adsorbed near the grain boundaries in thin-film gas sensors is active in modifying the electrical transport properties, which lose the large length-to-diameter and surface-to-volume ratios compared to bulk materials and films for nanostructure building block resulting from agglomeration [8]. In order to overcome these limitations, different types of nanostructured materials have been investigated for their gas response, gas response and other possible applications in sensors with better performances [9]. For example, the gas sensors fabricated by individual wire or rod extensively were used in an industrialized process as building block [10–12]. To achieve high current amplification and enhance signal-to-noise ratio, gas sensors relied on field-effect transistors (FETs) emerged [13–15]. These devices were fabricated by expensive and time consuming fabrication techniques, which very limited for practical applications. Array-based sensors open a new horizon for the investigation of high-performance sensors, and are considered as good candidates for gas sensors because of low cost and great miniaturization potential. Meanwhile, their low density and large surface-area-to-volume ratio facilitate diffusion of gases into and from the nanostructure. Moreover, a lower detection limit can be achieved because of a larger change in their electronic properties upon surface adsorption [16–18].

Zinc oxide (ZnO), an important and promising functional metal oxide semiconductor material with a direct wide band gap ($E_g \approx 3.37$ eV) and large exciton bonding energy (~60 meV), has been investigated extensively in many areas, such as light-emitting diodes, solar cells, photodetectors, heterogeneous catalysis, piezoelectric transducers and gas sensors [19–23]. Particularly, ZnO is one of the most promising materials for gas sensor application due to its high mobility of conduction electrons and good chemical and thermal stability. The gas sensing properties of ZnO depend strongly on its morphology including aspect ratio, size, orientation

* Corresponding author. Tel.: +86 571 87953139; fax: +86 571 87952625.
E-mail address: zlp1@zju.edu.cn (L. Zhu).

http://dx.doi.org/10.1016/j.snb.2014.11.024
0925-4005/© 2014 Elsevier B.V. All rights reserved.

and density of the crystal [24]. Over the past decades, considerable efforts have been made to improve the gas response, speed of response and stability of ZnO based gas sensors through modulating the microstructure, for example, nanograined nanowires [25], hierarchically assembled nanoflakes [26], porous microtubes [27], *etc*. Among these, ZnO arrays have been demonstrated to be an optimized architecture for boosting gas-sensing performance. Previously, Zeng et al. fabricated thin film gas sensors based on a ZnO nanorod arrays with high-performance ethanol detection [28]. Hassan's group reported a high-sensitivity room-temperature hydrogen gas sensor based on oblique and vertical ZnO nanorod arrays [29,30]. Sun et al. prepared tubular ZnO microstructure arrays and then constructed a gas sensor for CO detection [31]. On the other hand, porous ZnO nanostructures have also drawn extensive research attention due to their porous structured networks and high internal surface area, which result in the enhancement of gas sensing performance. Specifically, the introduction of pores into ZnO nanostructures facilitates the gas diffusion and mass transport, enormously improving gas sensor performance, such as nest-like ZnO hierarchically porous structures [32], porous and single crystalline ZnO nanosheets [33], hollow and mesoporous ZnO microsphere [34], *etc*. Nevertheless, the reports about porous ZnO arrays for gas sensing application are rare.

In this work, we present the fabrication of the mesoporous rhombus-shaped ZnO rod arrays based gas sensor. The synthesis includes the low temperature fluorine-mediated hydrothermal route of preparing rhombic Zn(OH)F rod arrays and then thermal conversion to mesoporous ZnO. Both precursor and gas-sensing materials were characterized by X-ray diffraction (XRD), thermogravimetric analysis (TGA), scanning electron microscopies (SEM), Fourier transform infrared spectroscopy (FTIR), N_2 physisorption, X-ray photoelectron spectroscopy (XPS) and Photoluminescence (PL). To evaluate the integrated properties of gas sensors, a series of detailed gas-sensing experiments were carried out. The obtained gas sensors annealing at different temperatures exhibited different gas-sensing performance toward ethanol detection, which are due to particle size distributions, specific surface areas and defects concentrations. The rhombus-shaped ZnO rod arrays based gas sensors show outstanding advantages, which can be attributed to the unique structure.

2. Experimental

2.1. Chemical materials

All chemicals or materials were of analytical grade and used directly without any further purification prior to usage. The zinc nitrate, ammonium fluoride, hexamethylenetetramine and urea were purchased from Shanghai Chemical Reagent Co. Ltd. Deionized water (18.3 MΩ cm resistivity) was produced by using a Millipore Direct-Q System, and used throughout the experiments. The polycrystalline alumina ceramic substrates shown in Fig. 1(a) were bought from Beijing Elite Tech Co., Ltd, China, which are $13.4 \times 7\ mm^2$, 0.5 cm in thick and plated five pairs Ag—Pd finger electrode regions.

2.2. Synthesis

The rhombus-shaped ZnO rod arrays were prepared via a two-step fluorine-mediated hydrothermal process reported by our previous work [35]. In a typical synthesis, a piece of substrate was firstly cleaned by a mixture of ethanol and acetone. Then, 200-nm-thick ZnO seed layers were deposited on the polycrystalline alumina ceramic substrate by radio-frequency magnetron sputtering using a ZnO target at 300 °C, 150 W, 1.0 Pa, 30 min. Afterwards,

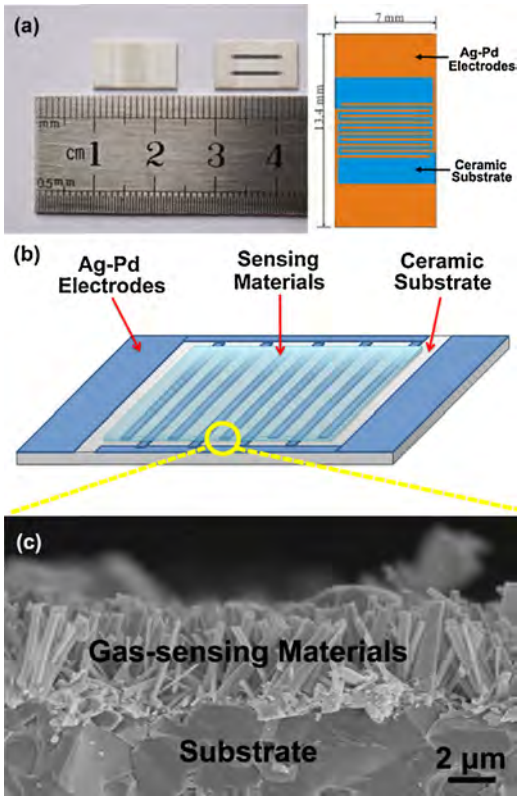

Fig. 1. (a) The photograph and schematic diagram of the polycrystalline alumina ceramic substrate; (b) schematic structure and (c) SEM image of the mesoporous rhombus-shaped ZnO rod arrays based gas sensor.

4 mmol $Zn(NO_3)_2{\cdot}6H_2O$, 8 mmol HMT and 16 mmol NH_4F were dissolved in 40 ml high purity water under stirring at room temperature. After stirring for 10 min, the homogeneous solution was transferred into a 50 ml Teflon-lined stainless steel autoclave. The prepared-substrate was immersed in the reaction solution leaning against the inner wall of the autoclave and fixed by polyimide tapes. The autoclave was sealed and maintained at 95 °C for 24 h inside an electric oven. After cooling down to room temperature, the substrate was removed, rinsed with distilled water several times, and dried at 60 °C under air condition for 2 h. Finally, the as-prepared precursors were converted to ZnO via thermal decomposition after annealing at 350, 450, 550 and 650 °C in air for 4 h, hereinafter designated as S350, S450, S550 and S650 samples, respectively. The obtained sensors were directly used for gas sensing measurements. Fig. 1(b) and (c) illustrates the structure of the rhombic ZnO nanorod arrays based gas sensors.

2.3. Characterization

The crystal phase identification of both the precursor and calcined products were investigated by X-ray diffraction (Bede D1) system with Cu-$K\alpha 1$ radiation ($\lambda = 0.15406$ nm). The morphologies were investigated using field emission scanning electron microscopy (Hitachi S-4800). Thermogravimetric analysis (TGA) was carried out using a TA Q600 instrument in a temperature range from 25 to 1000 °C with a heating rate of 10 °C/min in air. Fourier transform infrared spectroscopy (TENSOR 27) was characterized with DTGS detector by making pellets with KBr powder. Specific surface areas were computed from the results of N_2 physisorption at 77 K (TriStar II 3020) by using the BET (Brunauer–Emmett–Teller) and BJH (Barrett–Joyner–Halenda). X-ray photoelectron spectroscopy (Thermo ESCALAB 250) measurements were performed with a monochromatic Al-$K\alpha$ ($h\nu = 1486.6$ eV) X-ray source.

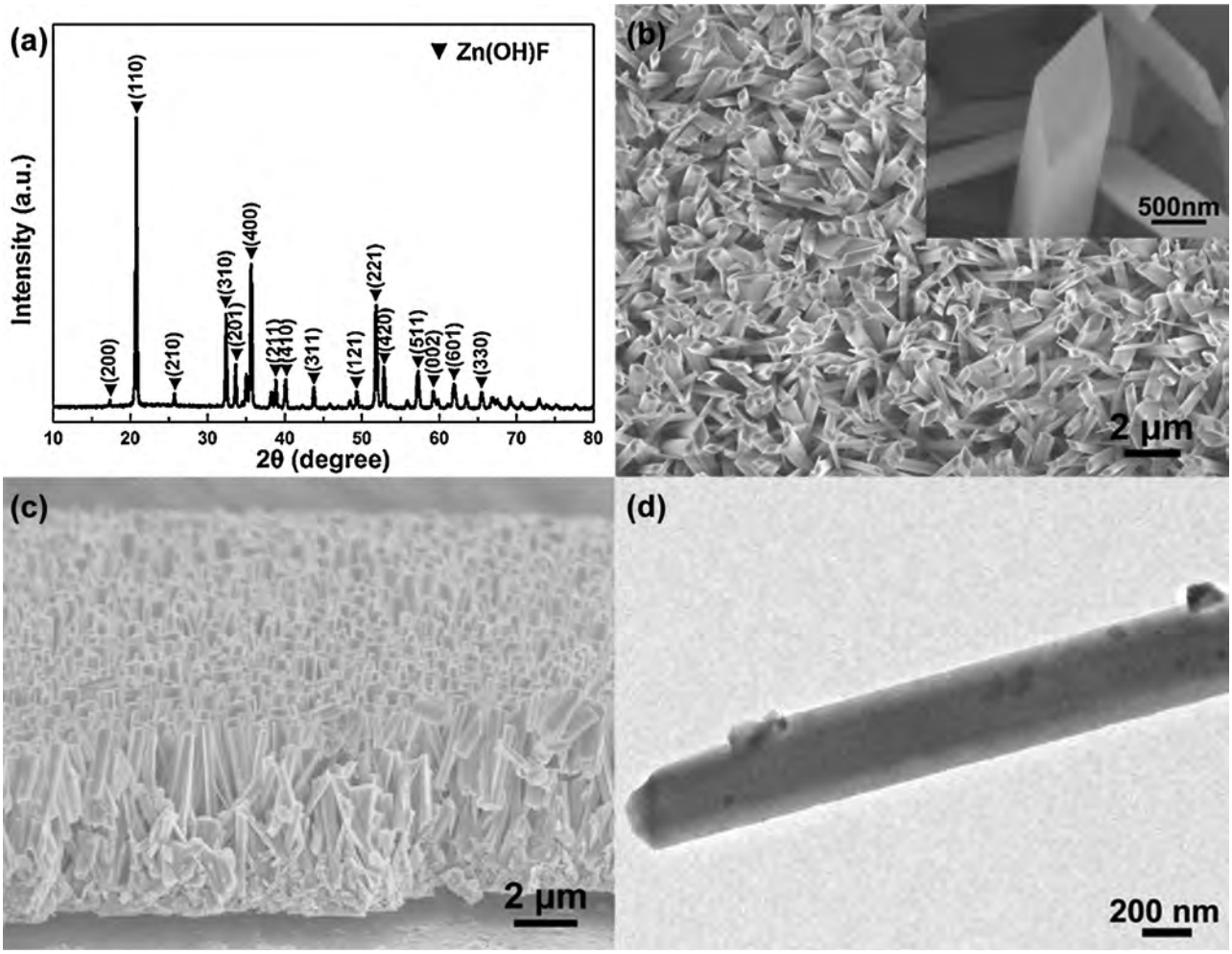

Fig. 2. Phase composition, morphological and structural characterization of the precursor Zn(OH)F: (a) XRD pattern; (b) top view of SEM image (inset shows a magnified rhombic shape); (c) cross-sectional SEM image of Zn(OH)F rod arrays growing on supporting substrate; and (d) TEM image of a single Zn(OH)F rod.

Photoluminescence spectra were recorded on a FLS920 fluorescence spectrometer (Edinburgh Instruments) with a 325 nm helium–cadmium laser as the excitation source equipped with a variable attenuator. The electrical characteristics were measured at room temperature in the dark using a semiconductor parameter analyzer (Agilent E5270B) with the bias voltage range of −10 to 10 V.

2.4. Gas-sensing measurement

The gas-sensing properties were performed on an intelligent gas sensing analysis system (CGS-1TP, Beijing Elite Tech Co., Ltd, China). The analysis system offered an external temperature control (from room temperature to 500 °C), which could conductively adjust the sensor temperature with a precision of 1 °C. The sensors were laid on the temperature control and pre-heated at different operating temperatures for about 30 min. Two probes were pressed on sensor electrodes by controlling the position adjustment in the analysis system. When the resistance of the sensor was stable, saturated target gas was injected into the test chamber (18 L in volume) by a micro-injector through a rubber plug. The saturated target gas was mixed with air (relative humidity was ~46%) by two fans. After the sensor resistance reached a new constant value, the test chamber was opened to recover the sensors in air. The sensor resistance and gas response were collected and analyzed by the system in real time. Gas response (S) was designated as the ratio R_a/R_g, where R_g is the sensor resistance of a mixture of target gas while R_a is in air. Response and recovery times are defined as the time needed for 90% of total resistance change on exposure to gas and air, respectively.

3. Results and discussion

The phase composition and morphology of the precursor obtained by the fluorine-mediated hydrothermal method were investigated firstly. Fig. 2(a) displays the XRD pattern of the powder from as-prepared precursor. All of the diffraction peaks in this pattern are in good agreement with a pure orthorhombic phase of Zn(OH)F (SG: $Pna2_1$, JCPDS 32-1469). The pattern shows very sharp peaks, indicating the precursor has good crystallinity. From a typical SEM image of the precursor in Fig. 2(b), we can see that large-scale and high density arrays of Zn(OH)F rods are uniformly grown on the substrate. The inset shows that the rod arrays have a clear-cut rhombic contour with an average edge length of ~400 nm and an induced edge angle of around 50°, and the surface of the rods is smooth. The cross-sectional SEM image in Fig. 2(c) reveals that the Zn(OH)F rod arrays with a length of about 4 μm are homogeneously well aligned. The typical TEM image in Fig. 2(d) indicates that a single rod of Zn(OH)F has a diameter of 400 nm with a smooth surface, consistent with the SEM result.

Fig. 3(a) shows the three-step weight loss as a function of temperature in TG and DTA analysis of the precursor Zn(OH)F under air flow with a rate of 10 °C/min. The first weight loss of 2.6%

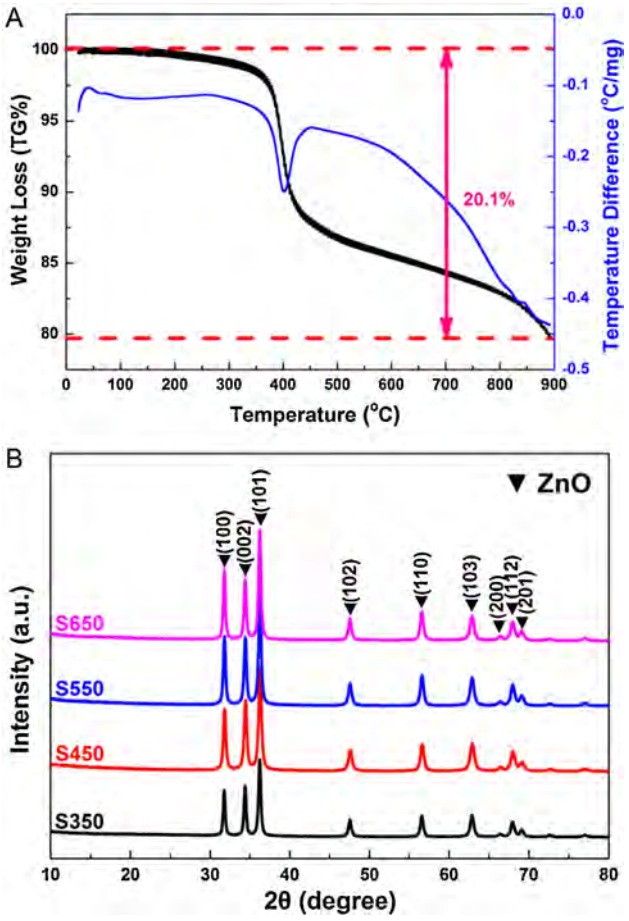

Fig. 3. (a) TG-DTA curves of the precursor Zn(OH)F. (b) XRD patterns of the rhombic ZnO rod arrays S350–S650, respectively.

below 350 °C is likely due to the evaporation of trapped solvent and adsorbed water. The second step occurs in the temperature range of 350–450 °C and shows an abrupt change with a weight loss of 9.6%, due to the decomposition of the precursor. After that, in the final step, the continued weight loss can be observed, owing to the weight loss of HF in thicker rods. As the temperature increased from room temperature to 900 °C, the total weight loss was approximately 20.1%, which is consistent with the theoretical value of 19.8% and indicates the decomposition of the precursor. From the known chemical composition of Zn(OH)F, the equation of decomposition reaction in the air can be inferred as the following (Eq. (1)):

$$\mathrm{Zn(OH)F} \rightarrow \mathrm{ZnO} + \mathrm{HF}\uparrow \quad (1)$$

To better understand the possible phase changes, the precursor Zn(OH)F were annealed at 350, 450, 550 and 650 °C for 4 h, respectively, to obtain ZnO. The phase structures of the samples after annealing at different temperature were analyzed systematically by XRD and FTIR, respectively. The XRD patterns in Fig. 3(b) reveals that all of the peaks of the four samples correspond well to wurtzite ZnO phase (SG: $P6_3mc$, JCPDS 36-1451) and no diffraction peaks of Zn(OH)F are observed, corroborating a crystal phase transformation from orthorhombic Zn(OH)F to hexagonal ZnO upon thermal treatment. The FTIR spectroscopy results (Fig. S1, Supplementary material) again confirmed the phase structure changes, in agreement with the XRD results.

To observe the detailed morphological and inner structural difference of the as-prepared rhombus-shaped ZnO rods, the high-magnification SEM images were prepared. Fig. 4 shows the significant changes of ZnO rods obtained at different annealing temperatures. From the low-magnification SEM image of S350 (Fig. S2, Supplementary material), we found no significant changes compared to the precursor. The high-magnification SEM image of S350 in Fig. 4(a) shows similar morphology to the precursor, which maintains the rhombic shape, however, with a coarse surface. From Fig. 4(b), it can be observed that the pores appeared on the surface of S450. A high-magnification SEM of the broken rod (Fig. S3, Supplementary material) displays that numerous nanopores exist in the rhombic building-block, arising from the transiton from Zn(OH)F to ZnO. This change leads to the formation of the porous ZnO through the thermal decomposition. The S550 can also maintain the original shape, which can be seen from Fig. 4(c), and larger pores are found on the surface. However, the morphology of the S650 has started to change because the rhombic rods consist of primary particles that fall into smaller grains, and the initial structures have collapsed, which are demonstrated in Fig. 4(d), and this change became clear for the sample annealed at 750 °C. The grains gather and recrystallize to a large irregular nanoparticle (Fig. S4, Supplementary material). The formation of the porous microstructure are due to the lattice contraction, pyrolysis and release of HF escaped from the inside of Zn(OH)F during the thermal treatment. Ostwald ripening can be used to interpret the growth of larger crystals from those of smaller size [36,37]. From these SEM images, it can be revealed that different surface morphologies of ZnO rods were obtained by thermal decomposition of the precursor Zn(OH)F at different temperatures, and the rods are porous.

To investigate further crystallographic properties of the rhombus-shaped ZnO rods, the typical TEM and HRTEM images of S450 were observed, as shown in Fig. 5. Similar to the results observed by SEM, the magnified TEM image in Fig. 5(a) indicates that a single rhombic ZnO rod has a diameter of ~400 nm and a porous structure with rough surfaces. An enlarged image of the individual rod shown in Fig. 5(b) reveals that the rod is composed of many tiny single crystals with different growth orientations. The ring-like selected-area electron diffraction (SAED) pattern (inset in Fig. 5b) clearly indicates the rhombic ZnO rod is polycrystalline in nature. The corresponding HRTEM observation further proves the polycrystalline structure. The HRTEM image in Fig. 5(c) taken from the area marked with a red square in Fig. 5(b) shows that no identical lattice fringes that generally reflect the crystal growth direction are clearly detected. These observation also confirmed the fabrication includes two steps, the low temperature fluorine-mediated hydrothermal route of preparing rhombic Zn(OH)F rod arrays and then thermal conversion to porous ZnO at different temperatures.

N_2 sorption measurements were evaluated for characterization of the textural properties and inner architectures of rhombic ZnO rods and gathering information about the specific surface area and pore size distribution. The N_2 absorption–desorption isotherms at 77 K are shown in Fig. 6. It can be observed that the isotherms of all four samples are characteristic of a type IV with type H3 hysteresis loop, which confirm the mesoporous structures [19,33]. The BET specific surface areas measurements were performed in a pressure range from 0.05 to 1.0, and for the samples S350 to S650 the calculated values were 35.4, 28.8, 21.1, and 12.8 $m^2\ g^{-1}$, respectively. Furthermore, the pore size distribution is shown in the insets of Fig. 6. When it comes to the temperature of 350 °C, the pore size distribution is not uniformly ranging from 3 to 40 nm and centered at 8.9 nm, which is caused by incomplete decomposition of precursors. With the temperature increasing to 450 °C, the pore size distribution reveals a bimodal nature with a narrow distribution centered at 3.9 nm and a wide distribution centered at 11.4 nm. The S550 sample shows a narrow pore size centered at 15.1 nm. After that, the remaining sample obtained at higher temperature does not expose the similar isotherms. The S650 sample reveals a relatively wide peak around from 10 to 60 nm and the central

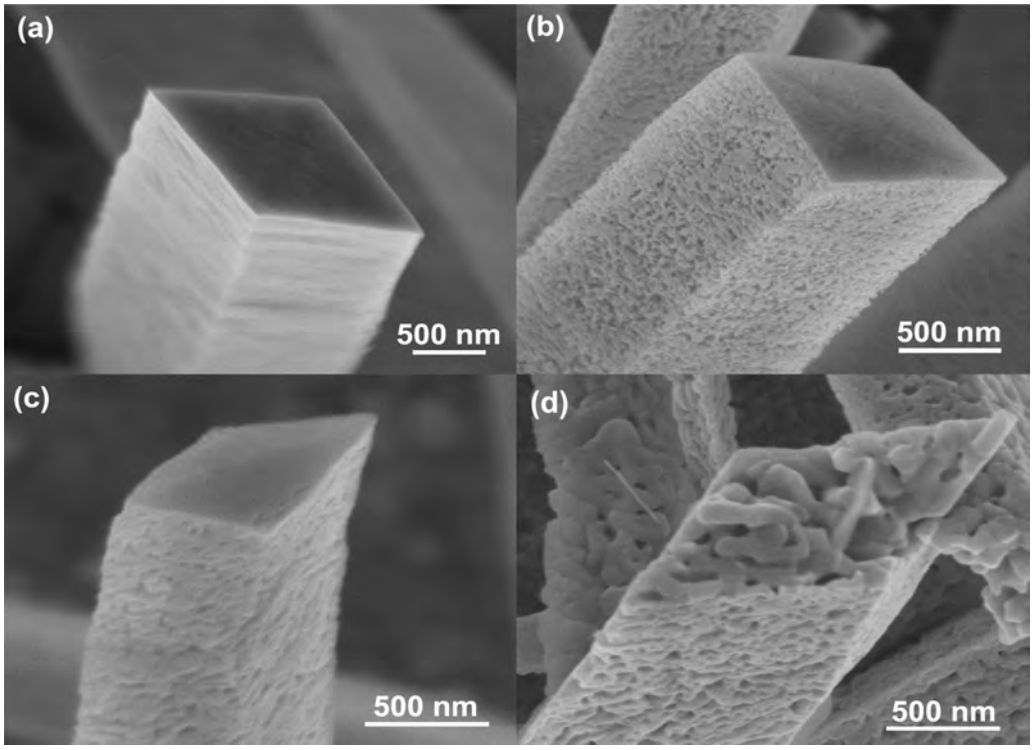

Fig. 4. High-magnification SEM images of the rhombic ZnO rods: (a) S350, (b) S450, (c) S550 and (d) S650.

value of distribution is 18.9 nm. These differences of BET surface area and pore size distribution may impact the gas-sensing properties of rhombus-shaped ZnO rod arrays. The observations from the N_2 sorption curves correspond well with the previous microscopy findings in Figs. 4 and 5.

For further investigation of the chemical composition of the as-prepared ZnO rods at different annealing temperatures, the XPS measurements were implemented. S350 was selected to carry out a wide scan between 0 and 1200 eV as shown in Fig. 7(a), since this sample was achieved at a low temperature and might contain lots of components. The binding energies in the XPS analyses are corrected for specimen charging by referring the C *1s* peak to 284.8 eV. The peaks at 284.8, 530.2, 684.2, and 1021.3 eV are indexed to the characteristic peaks of C *1s*, O *1s*, F *1s* and Zn $2p_{3/2}$, respectively. Fig. 7(b) shows the spectra of Zn $2p_{3/2}$ of four samples. A strong peak appeared at about 1021.3 eV corresponds to the data for standard ZnO spectra [38]. The major peak of O *1s* observed in Fig. 7(c) is 530.2 eV, which can be attributed to the lattice oxygen of ZnO. Besides, a small broadening peak centered at 532.0 eV corresponds to the absorbed species at the surface [39]. The F *1s* sharp peak in Fig. 7(d) at 684.2 eV can be assigned to the lattice fluorine of Zn(OH)F, and the fluorine content of the other samples can be neglected compared to S350 [40]. The presence of fluorine elements may be related with the incomplete decomposition of Zn(OH)F in the heat treatment, which may affect the gas-sensing property of the rhombic ZnO rod arrays.

The room temperature PL spectra of the four samples are shown in Fig. 8. Typically, two emission bands have been observed in these rhombic ZnO rods. One is a weak ultraviolet peak at 385 nm, which corresponds to the excitonic recombination of the near-band edge (NBE) emission. The other is a broad visible peak located in the range of a defect related green-orange band (480–750 nm), which is ascribed to the defect states, such as oxygen vacancies, zinc vacancies, interstitial zinc and interstitial oxygen [41,42]. In this plot, all spectra were normalized to NBE peak. Although these samples were prepared under the same condition, there were significant variations in the defect-related emissions intensity. The resulting defect-related emissions of S350 sample generally occur near the yellow (590 nm) regions. As the annealing temperature increases, a considerable red shift of the peak (from 590 to 610 nm) can be observed. Commonly reported the orange-red emission was attributed to the excess oxygen on the ZnO surface, which depends

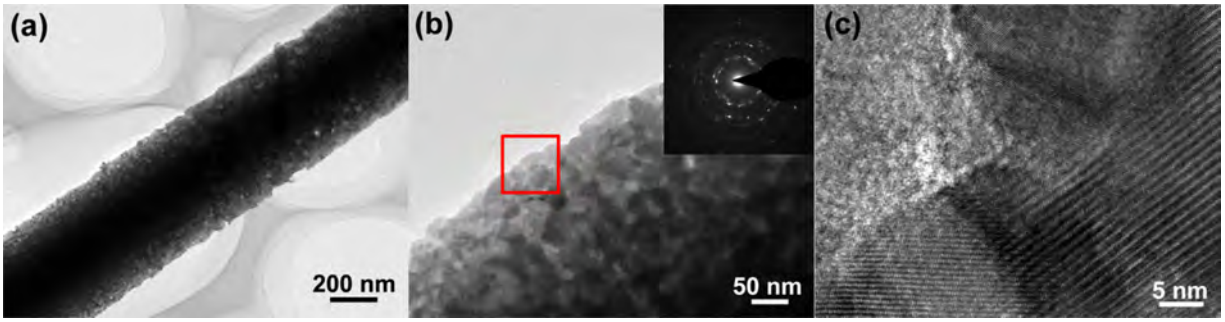

Fig. 5. (a) Low-magnification TEM image of a single NR of S450; (b) the enlarged TEM image of the individual NR (inset represents the SAED pattern); (c) HRTEM image taken from the area indicated by the red square in part b.

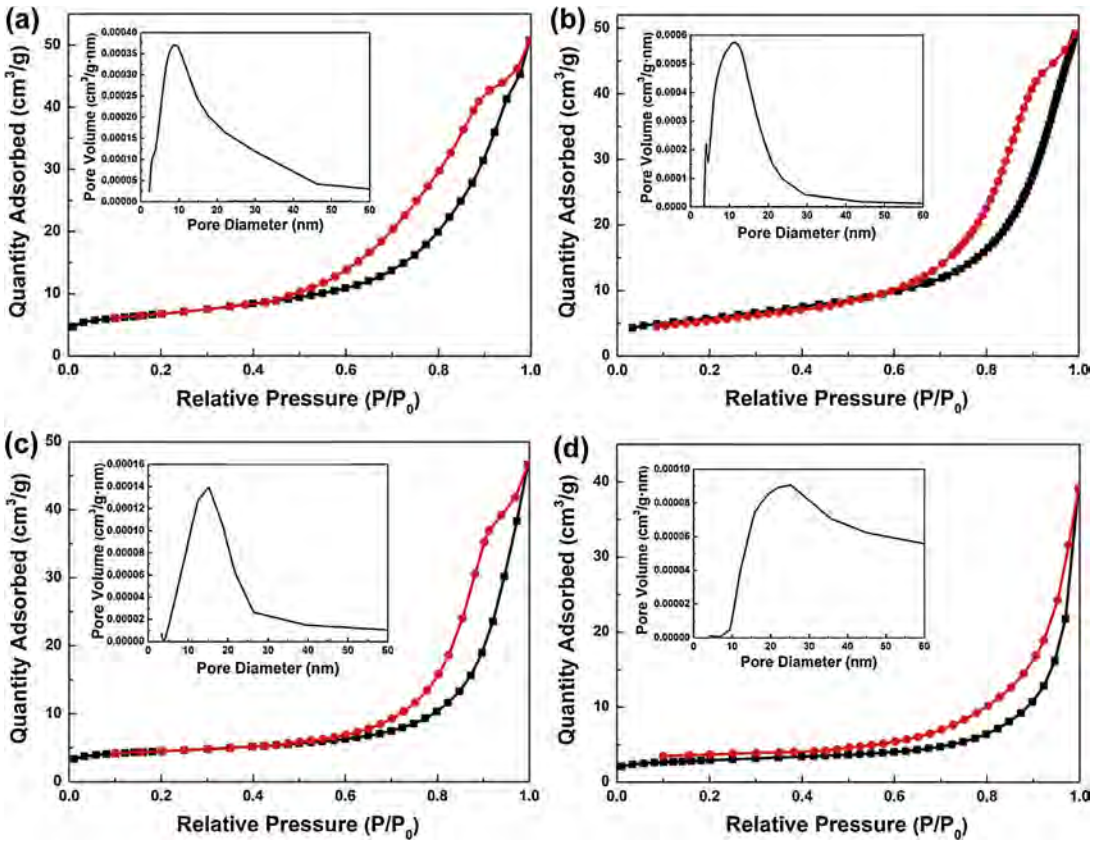

Fig. 6. N_2 adsorption/desorption isotherm (77 K) curves of rhombic ZnO rods and porous volume distribution of the pore size (the inset of each curve): (a) S350, (b) S450, (c) S550, and (d) S650.

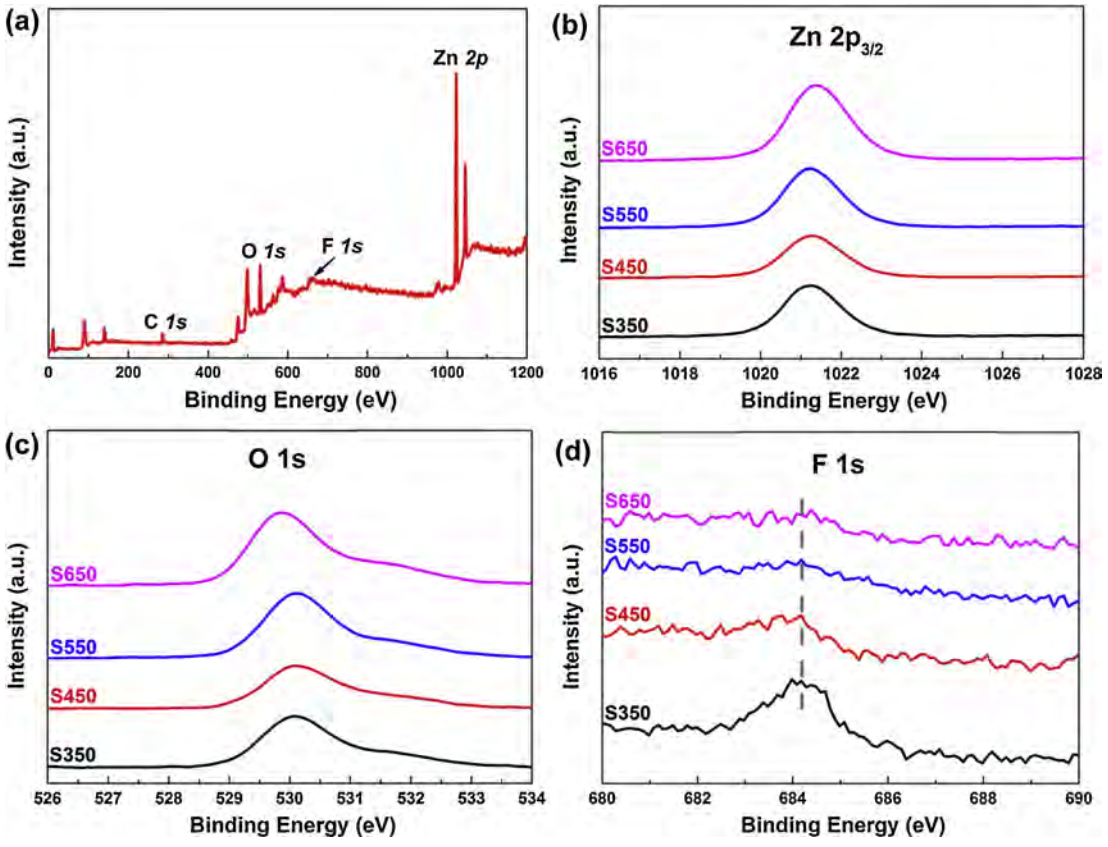

Fig. 7. XPS survey spectra of the rhombic ZnO rods: (a) wide scan of S350, (b) Zn $2p_{3/2}$, (c) O *1s*, and (d) F *1s*.

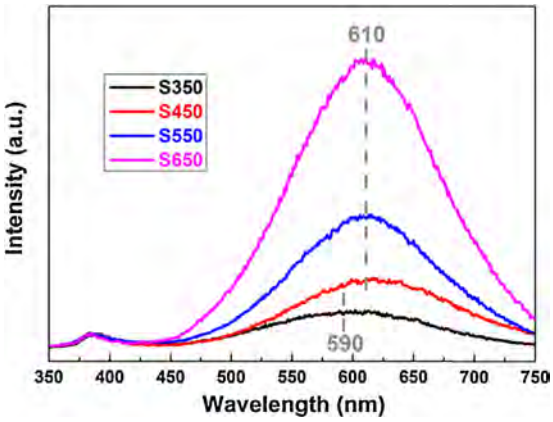

Fig. 8. Room-temperature photoluminescence spectrum of the rhombic ZnO rod arrays S350–S650, respectively.

on annealing and surface modifications [42,43]. The results reveal that as annealing temperature increases, larger amounts of interstitial oxygen exist on the surface of the rhombic rods. We consider the blue shift of S350 sample is due to the incomplete decomposition of Zn(OH)F (Fig. S5, Supplementary material).

Fig. 9 plots the typical current–voltage (*I–V*) characteristics between the two neighboring electrodes bridged by the rhombic ZnO rods in the air. The rods grown on the pre-deposition of seeds layers are randomly oriented, which provides electrical paths between the neighboring fingers. The current increased linearly with applied bias of all the *I–V* curves, revealing good Ohmic contacts between the ZnO rod arrays and the electrodes. It ensures that all upcoming behaviors of electrical devices represent the gas-sensing properties but not the contact between the materials and the electrodes [44,45]. On the basis of the above-mentioned discussion, we consider that it is possible to use the rhombic ZnO rod arrays directly as gas sensors without the complicated film formation process.

To evaluate the integrated properties of gas sensors, the optimal working temperature for maximum response was determined initially. Fig. 10 shows the gas sensing characteristics of the mesoporous rhombic ZnO rod arrays based gas sensors to 100 ppm ethanol at different working temperatures. The rhombic ZnO rod arrays based sensors utilize the change of surface electrical conductivity to detect gases, which results from the adsorption of the tested gas on the surface of the sensors [4,46]. It is evident that

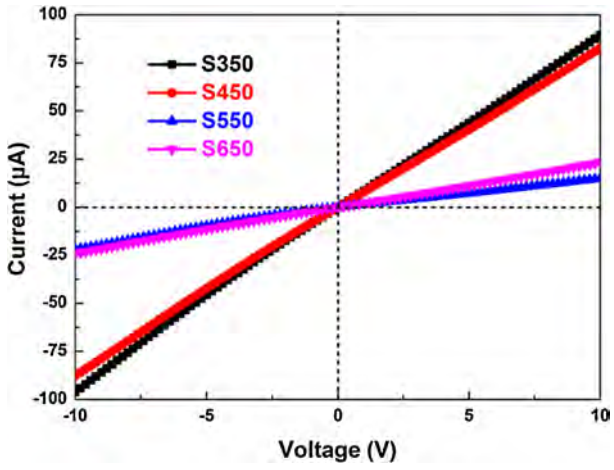

Fig. 9. *I–V* characteristics between the two neighboring electrodes bridged by the rhombic ZnO rod arrays S350–S650, respectively.

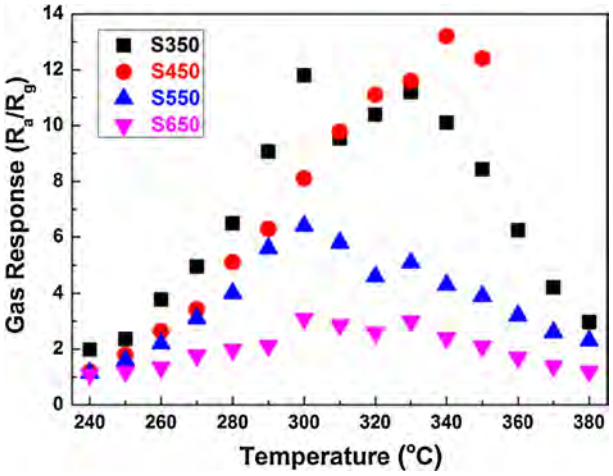

Fig. 10. Gas response of the rhombic ZnO rod arrays based gas sensor as a function of different working temperatures to 100 ppm ethanol.

different annealing temperatures lead to a different response to ethanol vapor. The sensor S350 shows the highest gas response at 340 °C and the response reaches ~13.2. However, the sensor showed very poor recovery property, reproducibility and stability (Fig. S6, Supplementary material). As annealing temperature increases, the sensors S450–S650 exhibit the declining gas response and show a double humped distribution with peaks at 300 °C and 330 °C, which is the typical performance of a surface-controlled gas sensor [47]. The S450 sample reaches the highest gas response at 300 °C and the gas response to 100 ppm ethanol is ~11.8. We attribute this behavior to larger grains and lower specific surface area at higher temperatures. Meanwhile, we suggest that the acceptor-related defects (oxygen interstitial) inhibit the free oxygen from being chemisorbed onto the ZnO surface and lead to lower gas response in the gas sensors [48,49]. Though having the highest gas response, the S350 sample showed an abnormal phenomenon, which is caused by the residual fluorine element in ZnO after calcination at low temperature. Therefore, annealing at 450 °C for the mesoporous rhombus-shaped ZnO rod arrays is suggested to be responsible for the optimal gas sensor. We can conclude that the performance of rhombic ZnO rod arrays based gas sensors is greatly influenced by their grain size distributions, specific surface area and defects concentration.

Thus, S450 sensor was selected to carry out a series of detailed gas-sensing experiments. Fig. 11(a) shows the typical response and recovery curves to ethanol with concentrations ranging from 10 to 500 ppm at 300 °C. The resistance underwent a drastic decrease on the injection of ethanol vapor and mostly recovered to its initial value after exposing gas to air, in agreement with a typical *n*-type semiconductor in the entire working temperature range [35]. Both response and recovery were very fast, taking about 4 and 7 s, respectively. After several cycles of gas injection, full recovery to the initial response of the gas sensors retains the same, indicating good reproducibility of the as-synthesized gas sensor. Fig. 11(b) shows the corresponding responses versus ethanol with concentrations ranging from 10 to 200 ppm. The well linear tendency in the range confirms that the sensor is quantitatively for a breath analyzer [50]. Fig. 11(c) shows the gas response to several 100 ppm reducing gases at 300 °C. The gas response to 100 ppm ethanol vapor is higher than all the other gases under the same concentration, showing high anti-interference ability. Further investigation of the long-term stability for real application was tested. The response of the sensor to 100 ppm ethanol is repeated for a period of 3 months with 30 times as shown in Fig. 11(d). The mean response and standard errors are calculated to be 11.8 and 1.01, showing a relative error of ~8.6%.

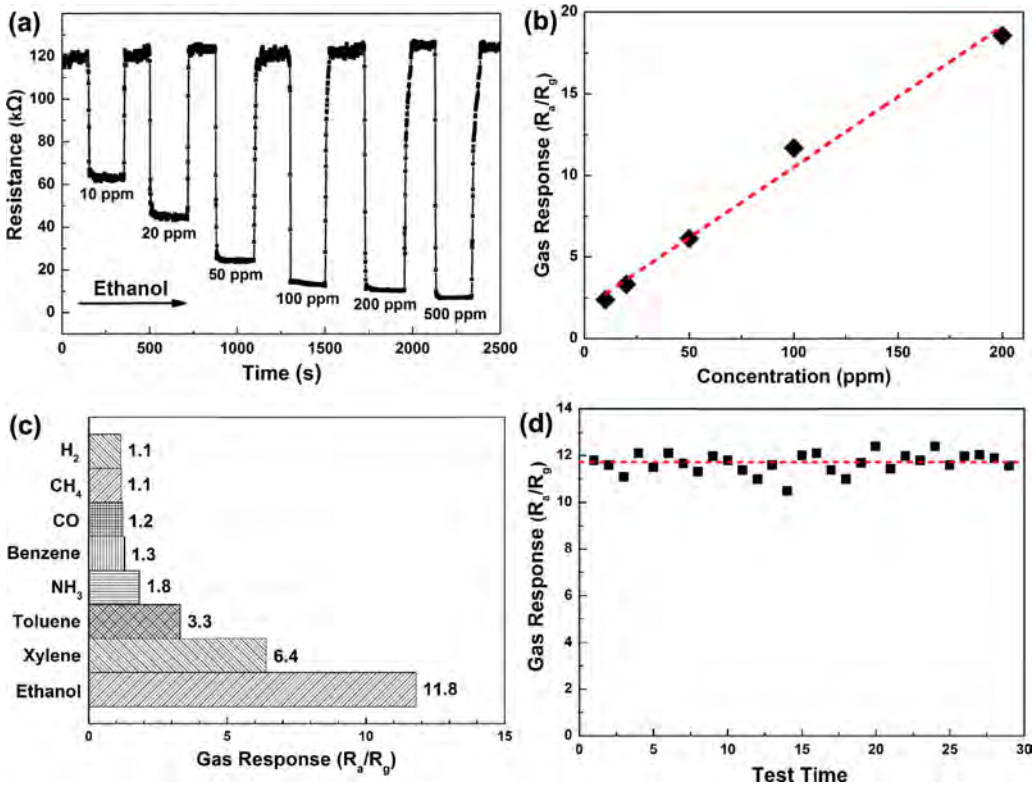

Fig. 11. The gas-sensing properties of the rhombic ZnO nanorod arrays based gas sensor at the working temperature of 300 °C: (a) representative response and recovery curve with concentration ranging from 10 to 500 ppm of ethanol; (b) responses to ethanol with concentrations ranging from 10 to 500 ppm; (c) selectivity with several reducing gases (100 ppm). (d) Responses to 100 ppm ethanol (RH ~ 46%) repeated with 30 times test during three months.

Therefore, we can summarize that the stability of this material is good enough in long time detection of ethanol.

Compared to the previous reports about ZnO arrays based gas sensors [16,51,52], the rhombus-shaped ZnO rod arrays based gas sensors show the advantages attributed to the unique structure with a variety of favorable features. First, numerous nanopores on the surface of rods during the thermal treatment increase the specific surface area tremendously. The high surface-to-volume ratio can provide more active reaction sites for adsorption and transportation of gas molecules. Moreover, the tunable pore size allows the gas molecules to easily penetrate and adsorb on the surface, leading to fast response and recovery as well as high gas response [3,53]. Second, the rhombic ZnO rods are polycrystalline in nature, which consists of a chain of many small grains, giving a relatively higher active surface area in comparison with a single-crystalline rod having the same average dimensions. Gas molecules could be stored in the interface and boundary of grains, thus enhancing the gas response [54,55]. Particularly, the high crystallinity of the ZnO rods dramatically increases the long-term stability of the devices [56]. Third, the PL results reveal that large amounts of point defects (Zn interstitials and O vacancies) are located on the surface of the rhombic rods. The surface defects often dominate the electronic/chemical properties and adsorption behaviors of metal oxide surfaces. This means the point defects bind more tightly with ethanol molecules attracting more charge from ZnO surfaces compared with defect-free ZnO surface, which is benefited for significantly enhancing gas response [57,58]. Fifth, the as-prepared rods can still stick to the substrate firmly even after strong ultrasonication over 30 min, suggesting the robust adhesion between the materials and the supporting substrate. Good Ohmic contact with the electrodes and intensive contact with the substrates make it possible to use the nanoarrays directly as gas sensors. The open space of the nanoarrays between individual rod allows for easy contact and diffusion of the gas molecular into the inner region of the rods and facilitates every rod to involve the gas sensing reaction [18,56].

4. Conclusions

In present work, we report a novel mesoporous rhombus-shaped ZnO rod arrays based gas sensor. The process involves the formation of rhombic Zn(OH)F rod arrays as precursor and then thermal conversion to mesoporous ZnO. The gas sensors annealing from 350 to 650 °C showed different gas response to 100 ppm ethanol, which can be attributed to different grain sizes, specific surface area and oxygen interstitial. The sensor annealing at 450 °C has the best performance, and the response to 100 ppm reached ~11.8 at 300 °C. The sensor also exhibited good response/recovery speed (4 s and 7 s), excellent gas response and good stability. Compared to traditional hexagonal ZnO rod arrays based gas sensor, the rhombic ZnO rod arrays exhibit entire advantages of porosity structure, large specific surface area, large amounts of point defects and good crystallinity.

Acknowledgements

This work was supported by National Natural Science Foundation of China (51372224), Program for Innovative Research Team in University of Ministry of Education of China (IRT13037), and National Science and Technology Support Program (2012BAC08B08). Zhen Wen would like to express his sincere gratitude to the China Scholarship Council (CSC) for the scholarship to help his study in the Georgia Institute of Technology, United States.

Appendix A. Supplementary data

Supplementary data associated with this article can be found, in the online version, at http://dx.doi.org/10.1016/j.snb.2014.11.024.

References

[1] T. Wagner, S. Haffer, C. Weinberger, D. Klaus, M. Tiemann, Mesoporous materials as gas sensors, Chem. Soc. Rev. 42 (2013) 4036–4053.
[2] N. Barsan, D. Koziej, U. Weimar, Metal oxide-based gas sensor research: how to? Sens. Actuators B: Chem. 121 (2007) 18–35.
[3] Y. Cui, Q. Wei, H. Park, C.M. Lieber, Nanowire nanosensors for highly sensitive and selective detection of biological and chemical species, Science 293 (2001) 1289–1292.
[4] L. Wang, Y. Kang, X. Liu, S. Zhang, W. Huang, S. Wang, ZnO nanorod gas sensor for ethanol detection, Sens. Actuators B: Chem. 162 (2012) 237–243.
[5] I.D. Kim, A. Rothschild, Nanostructured metal oxide gas sensors prepared by electrospinning, Polym. Adv. Technol. 22 (2011) 318–325.
[6] X.J. Huang, Y.K. Choi, Chemical sensors based on nanostructured materials, Sens. Actuators B: Chem. 122 (2007) 659–671.
[7] G. Sberveglieri, C. Baratto, E. Comini, G. Faglia, M. Ferroni, A. Ponzoni, A. Vomiero, Synthesis and characterization of semiconducting nanowires for gas sensing, Sens. Actuators B: Chem. 121 (2007) 208–213.
[8] H.N. Hieu, N.M. Vuong, H. Jung, D.M. Jang, D. Kim, H. Kim, S.K. Hong, Optimization of a zinc oxide urchin-like structure for high-performance gas sensing, J. Mater. Chem. 22 (2012) 1127–1134.
[9] M.W. Ahn, K.S. Park, J.H. Heo, D.W. Kim, K.J. Choi, J.G. Park, On-chip fabrication of ZnO-nanowire gas sensor with high gas sensitivity, Sens. Actuators B: Chem. 138 (2009) 168–173.
[10] S.N. Das, J.P. Kar, J.H. Choi, T. Il Lee, K.J. Moon, J.M. Myoung, Fabrication and characterization of ZnO single nanowire-based hydrogen sensor, J. Phys. Chem. C 114 (2010) 1689–1693.
[11] O. Lupan, L. Chow, G. Chai, A single ZnO tetrapod-based sensor, Sens. Actuators B: Chem. 141 (2009) 511–517.
[12] L. Liao, H.X. Mai, Q. Yuan, H.B. Lu, J.C. Li, C. Liu, C.H. Yan, Z.X. Shen, T. Yu, Single CeO_2 nanowire gas sensor supported with Pt nanocrystals: gas sensitivity, surface bond states, and chemical mechanism, J. Phys. Chem. C 112 (2008) 9061–9065.
[13] T.Y. Wei, P.H. Yeh, S.Y. Lu, Z.L. Wang, Gigantic enhancement in sensitivity using Schottky contacted nanowire nanosensor, J. Am. Chem. Soc. 131 (2009) 17690–17695.
[14] Z. Fan, D. Wang, P.C. Chang, W.Y. Tseng, J.G. Lu, ZnO nanowire field-effect transistor and oxygen sensing property, Appl. Phys. Lett. 85 (2004) 5923–5925.
[15] H. Yoon, S. Ko, J. Jang, Field-effect-transistor sensor based on enzyme-functionalized polypyrrole nanotubes for glucose detection, J. Phys. Chem. B 112 (2008) 9992–9997.
[16] S. Ma, R. Li, C. Lv, W. Xu, X. Gou, Facile synthesis of ZnO nanorod arrays and hierarchical nanostructures for photocatalysis and gas sensor applications, J. Hazard. Mater. 192 (2011) 730–740.
[17] P. Offermans, M. Crego-Calama, S.H. Brongersma, Gas detection with vertical InAs nanowire arrays, Nano Lett. 10 (2010) 2412–2415.
[18] J.X. Wang, X.W. Sun, Y. Yang, H. Huang, Y.C. Lee, O.K. Tan, L. Vayssieres, Hydrothermally grown oriented ZnO nanorod arrays for gas sensing applications, Nanotechnology 17 (2006) 4995–4998.
[19] L. Wang, X. Zhang, K. Chen, Nano-scaled hierarchical porous ZnO nanostructures: fabrication and application in dye-sensitized solar cells, CrystEngComm 15 (2013) 4860–4864.
[20] S. Park, S. An, Y. Mun, C. Lee, UV-enhanced NO_2 gas sensing properties of SnO_2-core/ZnO-shell nanowires at room temperature, ACS Appl. Mater. Interfaces 5 (2013) 4285–4292.
[21] B. Liu, J. Xu, S. Ran, Z. Wang, D. Chen, G. Shen, High-performance photodetectors, photocatalysts, and gas sensors based on polyol reflux synthesized porous ZnO nanosheets, CrystEngComm 14 (2012) 4582–4588.
[22] M.H. Zhao, Z.L. Wang, S.X. Mao, Piezoelectric characterization of individual zinc oxide nanobelt probed by piezoresponse force microscope, Nano Lett. 4 (2004) 587–590.
[23] M. Chen, Z. Wang, D. Han, F. Gu, G. Guo, High-sensitivity NO_2 gas sensors based on flower-like and tube-like ZnO nanomaterials, Sens. Actuators B: Chem. 157 (2011) 565–574.
[24] S. Cho, S. Kim, D.W. Jung, K.H. Lee, Formation of quasi-single crystalline porous ZnO nanostructures with a single large cavity, Nanoscale 3 (2011) 3841–3848.
[25] S. Park, S. An, H. Ko, C. Jin, C. Lee, Synthesis of nanograined ZnO nanowires and their enhanced gas sensing properties, ACS Appl. Mater. Interfaces 4 (2012) 3650–3656.
[26] A. Sinhamahapatra, A.K. Giri, P. Pal, S.K. Pahari, H.C. Bajaj, A.B. Panda, A rapid and green synthetic approach for hierarchically assembled porous ZnO nanoflakes with enhanced catalytic activity, J. Mater. Chem. 22 (2012) 17227–17235.
[27] A.K. Giri, A. Sinhamahapatra, S. Prakash, J. Chaudhari, V.K. Shahi, A.B. Panda, Porous ZnO microtubes with excellent cholesterol sensing and catalytic properties, J. Mater. Chem. A 1 (2013) 814–822.
[28] S. Tian, F. Yang, D. Zeng, C. Xie, Solution-processed gas sensors based on ZnO nanorods array with an exposed (0001) facet for enhanced gas-sensing properties, J. Phys. Chem. C 116 (2012) 10586–10591.
[29] J.J. Hassan, M.A. Mahdi, C.W. Chin, H. Abu-Hassan, Z. Hassan, A high-sensitivity room-temperature hydrogen gas sensor based on oblique and vertical ZnO nanorod arrays, Sens. Actuators B: Chem. 176 (2013) 360–367.
[30] J.J. Hassan, M.A. Mahdi, C.W. Chin, H. Abu-Hassan, Z. Hassan, Room temperature hydrogen gas sensor based on ZnO nanorod arrays grown on a SiO_2/Si substrate via a microwave-assisted chemical solution method, J. Alloys Compd. 546 (2013) 107–111.
[31] J.X. Wang, X.W. Sun, H. Huang, Y.C. Lee, O.K. Tan, M.B. Yu, G.Q. Lo, D.L. Kwong, A two-step hydrothermally grown ZnO microtube array for CO gas sensing, Appl. Phys. A 88 (2007) 611–615.
[32] X. Wang, W. Liu, J. Liu, F. Wang, J. Kong, S. Qiu, C.Z. He, L.Q. Luan, Synthesis of nestlike ZnO hierarchically porous structures and analysis of their gas sensing properties, ACS Appl. Mater. Interfaces 4 (2012) 817–825.
[33] Y. Xiao, L. Lu, A. Zhang, Y. Zhang, L. Sun, L. Huo, F. Li, Highly enhanced acetone sensing performances of porous and single crystalline ZnO nanosheets: high percentage of exposed (100) facets working together with surface modification with Pd nanoparticles, ACS Appl. Mater. Interfaces 4 (2012) 3797–3804.
[34] J. Rao, A. Yu, C. Shao, X. Zhou, Construction of hollow and mesoporous ZnO microsphere: a facile synthesis and sensing property, ACS Appl. Mater. Interfaces 4 (2012) 5346–5352.
[35] Z. Wen, L. Zhu, L. Li, L. Sun, H. Cai, Z. Ye, A fluorine-mediated hydrothermal method to synthesize mesoporous rhombic ZnO nanorod arrays and their gas sensor application, Dalton Trans. 42 (2013) 15551–15554.
[36] H. Yu, D. Wang, M.-Y. Han, Top-down solid-phase fabrication of nanoporous cadmium oxide architectures, J. Am. Chem. Soc. 129 (2007) 2333–2337.
[37] F.J. Sheini, M.A. More, S.R. Jadkar, K.R. Patil, V.K. Pillai, D.S. Joag, Observation of photoconductivity in Sn-doped ZnO nanowires and their photoenhanced field emission behavior, J. Phys. Chem. C 114 (2010) 3843–3849.
[38] X. Hou, F. Zhou, W. Liu, A facile low-cost synthesis of ZnO nanorods via a solid-state reaction at low temperature, Mater. Lett. 60 (2006) 3786–3788.
[39] C. Chen, H. He, Y. Lu, K. Wu, Z. Ye, Surface passivation effect on the photoluminescence of ZnO nanorods, ACS Appl. Mater. Interfaces 5 (2013) 6354–6359.
[40] Y. Peng, H.Y. Zhou, Z.H. Wang, Synthesis, characterization and photocatalytic activity of Zn(OH)F hierarchical nanofibers prepared by a simple solution-based method, CrystEngComm 14 (2012) 2812–2816.
[41] P. Jiang, J.J. Zhou, H.F. Fang, C.Y. Wang, Z.L. Wang, S.S. Xie, Hierarchical shelled ZnO structures made of bunched nanowire arrays, Adv. Funct. Mater. 17 (2007) 1303–1310.
[42] M. Dai, F. Xu, Y. Lu, Y. Liu, Y. Xie, Synthesis of submicron rhombic ZnO rods via ZnOHF intermediate using electrodeposition route, Appl. Surf. Sci. 257 (2011) 3586–3591.
[43] C. Chen, Y. Lu, H. He, M. Xiao, Z. Wang, L.X. Chen, Z.Z. Ye, Violet emission in ZnO nanorods treated with high-energy hydrogen plasma, ACS Appl. Mater. Interfaces 5 (2013) 10274–10279.
[44] Z. Wen, L. Zhu, W. Mei, L. Hu, Y. Li, L. Sun, H. Cai, Z. Ye, Rhombus-shaped Co_3O_4 nanorod arrays for high-performance gas sensor, Sens. Actuators B: Chem. 186 (2013) 172–179.
[45] Z. Wen, L. Zhu, W. Mei, Y. Li, L. Hu, L. Sun, W. Wan, Z. Ye, A facile fluorine-mediated hydrothermal route to controlled synthesis of rhombus-shaped Co_3O_4 nanorod arrays and their application in gas sensing, J. Mater. Chem. A 1 (2013) 7511–7518.
[46] Z. Wen, L. Zhu, Y. Li, Z. Zhang, Z. Ye, Mesoporous Co_3O_4 nanoneedle arrays for high-performance gas sensor, Sens. Actuators B: Chem. 203 (2014) 873–879.
[47] X. Jia, H. Fan, M. Afzaal, X. Wu, P. O'Brien, Solid state synthesis of tin-doped ZnO at room temperature: characterization and its enhanced gas sensing and photocatalytic properties, J. Hazard. Mater. 193 (2011) 194–199.
[48] D.T. Phan, G.S. Chung, Effects of defects in Ga-doped ZnO nanorods formed by a hydrothermal method on CO sensing properties, Sens. Actuators B: Chem. 187 (2013) 191–197.
[49] N. Han, X.F. Wu, L.Y. Chai, H.D. Liu, Y.F. Chen, Counterintuitive sensing mechanism of ZnO nanoparticle based gas sensors, Sens. Actuators B: Chem. 150 (2010) 230–238.
[50] A. Star, V. Joshi, S. Skarupo, D. Thomas, J.C.P. Gabriel, Gas sensor array based on metal-decorated carbon nanotubes, J. Phys. Chem. B 110 (2006) 21014–21020.
[51] L.J. Bie, X.N. Yan, J. Yin, Y.Q. Duan, Z.H. Yuan, Nanopillar ZnO gas sensor for hydrogen and ethanol, Sens. Actuators B: Chem. 126 (2007) 604–608.
[52] T.J. Hsueh, C.L. Hsu, S.J. Chang, I.C. Chen, Laterally grown ZnO nanowire ethanol gas sensors, Sens. Actuators B: Chem. 126 (2007) 473–477.
[53] K.I. Choi, H.R. Kim, K.M. Kim, D. Liu, G. Cao, J.H. Lee, C_2H_5OH sensing characteristics of various Co_3O_4 nanostructures prepared by solvothermal reaction, Sens. Actuators B: Chem. 146 (2010) 183–189.
[54] J. Liu, Z. Guo, K. Zhu, W. Wang, C. Zhang, X. Chen, Highly porous metal oxide polycrystalline nanowire films with superior performance in gas sensors, J. Mater. Chem. 21 (2011) 11412–11417.
[55] N.L. Hung, H. Kim, S.K. Hong, D. Kim, A simple fabrication method of randomly oriented polycrystalline zinc oxide nanowires and their application to gas sensing, Adv. Nat. Sci.: Nanosci. Nanotechnol. 2 (2011) 015002.
[56] H. Nguyen, S.A. El-Safty, Meso- and macroporous Co_3O_4 nanorods for effective VOC gas sensors, J. Phys. Chem. C 115 (2011) 8466–8474.
[57] M.W. Ahn, K.S. Park, J.H. Heo, J.G. Park, D.W. Kim, K.J. Choi, J.H. Lee, S.H. Hong, Gas sensing properties of defect-controlled ZnO-nanowire gas sensor, Appl. Phys. Lett. 93 (2008) 263103–263106.
[58] R. Schaub, E. Wahlstrom, A. Ronnau, E. Lagsgaard, I. Stensgaard, F. Besenbacher, Oxygen-mediated diffusion of oxygen vacancies on the TiO_2 (110) surface, Science 299 (2003) 377–379.

Biographies

Zhen Wen received his BS degree at China University of Mining and Technology in 2011. He pursued his Ph.D. degree at Zhejiang University since 2011. Now he is a visiting Ph.D. student at Georgia Institute of Technology through the program of China Scholarship Council. His research interests are in the area of nano materials and nano energy.

Liping Zhu received her B.Sc. (1988) and M.Sc. (1991) degrees in Materials Science from Zhejiang University. She studied in Hiroshima University in Japan as a doctoral student from 1998 to 2002. Then she joined the Materials Department of Zhejiang University since 2002. Her current research interests include semiconductor materials, photo-electronic thin films, nano-materials and their application in devices.

Ziyue Zhang received BS degree at Northwestern Polytechnical University in 2013. She is currently pursuing Ph.D. degree at Zhejiang University. Her current fields of interests include design and synthesis of nano-materials and study their gas sensing properties.

Zhizhen Ye received his BS degree in Electrical Engineering, received his MS degree and his Ph.D. in Optical Engineering from Zhejiang University in 1981, 1984 and 1987 respectively. He has been a Professor of Materials Science and Engineering since 1994. His research interests are in the area of heterogrowth and devices fabrication of silicon-based thin films.